1 # High-resolution induced polarization imaging of biogeochemical

2 # carbon-turnover hot spots in a peatland

4 Timea Katona[1], Benjamin Silas Gilfedder[2], Sven Frei[2], Matthias Bücker[3], and Adrian Flores-Orozco[1]

6 (1) Research Division Geophysics, Department of Geodesy and Geoinformation, TU-Wien, Austria;

7 (2) Department of Hydrology, University of Bayreuth, Germany;

8 (3) Institute for Geophysics and Extraterrestrial Physics, TU Braunschweig, Germany

10 **Abstract**

11 Biogeochemical hot spots are defined as areas where biogeochemical processes occur with
12 anomalously high reaction rates relative to their surroundings. Due to their importance in carbon
13 and nutrient cycling, characterization of hot spots is critical to accurately predict carbon budgets
14 in the context of climate change. However, biogeochemical hot spots are difficult to identify in
15 the environment, as sampling resolutions are often too coarse to find these areas in the
16 subsurface. Here, we present imaging results of a geophysical survey using the non-invasive
17 induced polarization (IP) method to identify biogeochemical hot spots of carbon turnover in a
18 minerotrophic wetland. To interpret the field-scale IP signatures, geochemical analyses were
19 performed on freeze-core samples obtained in areas characterized by anomalously high and low
20 IP responses. Our results reveal large variations in the electrical response, with the highest IP
21 phase values (> 20 mrad) corresponding with high concentrations of phosphates (>4000 μM),
22 an indicator of carbon turnover. Moreover, analysis of the freeze core reveal negligible
23 concentrations of iron sulfides. The extensive geochemical and geophysical data presented in
24 our study demonstrates that IP images can assess changes in the biogeochemical activity in
25 peat, and identify hot spots.

26 **Keywords:** biogeochemical carbon turnover; geophysical imaging methods; electrical
27 conductivity; induced polarization; microbiologically active zones

1 Introduction

In terrestrial and aquatic ecosystems 'patches' or areas that show disproportionally high biogeochemical reaction rates relative to the surrounding matrix are referred to as biogeochemical 'hot spots' (McClain et al., 2003). Hot spots for turnover of redox-sensitive species (e.g. oxygen, nitrate or dissolved organic carbon) are often generated at interfaces between oxic and annoxic environments, where the local presence/absence of oxygen either favours or suppresses biogeochemical reactions such as aerobic respiration, denitrification or oxidation/reduction of iron (McClain et al., 2003). Biogeochemical hot spots are important for nutrient and carbon cycling in various systems such as wetlands (Frei et al., 2010; 2012), lake sediments (Urban, 1994), the vadose zone (Hansen et al., 2014), hyporheic areas (Boano et al., 2014) or aquifers (Gu et al., 1998). Wetlands are distinct elements in the landscape, which are often located where various hydrological flow paths converge, such as at the bottoms of basin shaped catchments, local depressions or around rivers and streams (Cirmo and McDonell 1997). Wetlands are attracting increasing interest because of their important contribution to water supply, water quality, nutrient cycling, and biodiversity (Costanza et al., 1997; 2017). Understanding microbial moderated cycling of nutrients and carbon in wetlands is critical, as these systems store a significant part of the global carbon through the accumulation of decomposed plant material (Kayranli et al., 2010). In wetlands, water table fluctuations as well as plant roots determine the vertical and horizontal distribution of oxic and anoxic areas (Frei et al., 2012; Gutknecht et al., 2006). Small scale subsurface flow processes in wetlands, moderated by micro-topographical structures (hollow and hummocks) (Diamond et al., 2020), can control the spatial presence of redox-sensitive solutes and formation of biogeochemical hot spots (Frei et al., 2010; 2012). Despite their relevance for the carbon and nutrient cycles, the field observations of the basic mechanisms controlling the formation and distribution of biogeochemical hot spots in space is largely missing.

Biogeochemical active areas traditionally have been identified and localized through chemical analyses of point samples from the subsurface and then subsequent interpolation of the data in space (Morse et al., 2014; Capps and Flecker, 2013; Hartley and Schlesinger, 2000). However, such point-based sampling methods may either miss hot spots due to the low spatial resolution of sampling (McClain et al., 2003) or disturb the redox-sensitive conditions in the subsurface by bringing oxygen into anoxic areas during sampling. Non-invasive methods, such as geophysical techniques, have the potential to study biogeochemical hot spots in-situ without interfering with the subsurface environment (e.g., Williams et al., 2005; 2009; Atekwana and Slater 2009; Flores Orozco et al., 2015; 2019; 2020). Geophysical methods permit to map large

63 areas in 3D and still resolve subsurface physical properties with a high spatial resolution (Binley

64 et al., 2015).

65 In particular, the induced polarization (IP) technique has recently emerged as a useful tool to

66 delineate biogeochemical processes in the subsurface (e.g., Kemna et al., 2012; Kessouri et al.,

67 2019; Flores Orozco et al., 2020). The IP method provides information about the electrical

68 conductivity and the capacitive properties of the ground, which can be expressed, respectively,

69 in terms of the real and imaginary components of the complex resistivity (Binley and Kemna,

70 2005). The method is commonly used to explore metallic ores because of the strong polarization

71 response associated to metallic minerals (e.g., Marshall and Madden, 1959; Seigel et al., 2007).

72 Pelton et al. (1978) and Wong (1979) proposed the first models linking the IP response to the

73 size and content of metallic minerals. More recently, the role of chemical and textural properties

74 in the polarization of metallic minerals has been investigated in detail (Revil et al., 2012, 2015a;

75 2015b, Bücker et al., 2018; 2019). In porous media without a significant metallic content, the

76 IP response can be related to the polarization of the electrical double layer formed at the grain-

77 fluid interface (e.g., Waxman and Smits, 1968; Revil and Florsch, 2010; Revil, 2012). In

78 particular, Revil et al. (2017) carried out complex conductivity measurements on a large set of

79 soil samples, for which they report a linear relation between the magnitude of the polarization

80 response and the cation exchange capacity (CEC), which in turn is related to surface area and

81 surface charge density.

82 Since the early 2010s, various studies have explored the potential of IP measurement for the

83 investigation of biogeochemical processes (Slater and Attekwana, 2013). Laboratory studies on

84 sediment samples examined the correlation between the spectral induced polarization (SIP)

85 response and X iron sulfid precipitation caused by iron reducing bacteria (Williams et al., 2005;

86 Ntarlagiannis et al., 2005; 2010; Slater et al., 2007; Personna et al., 2008; Zhang et al., 2010;

87 Placencia Gomez et al., 2013; Abdel Aal et al., 2014). Further investigations in the laboratory

88 have also revealed an increase in the polarization response accompanying the accumulation of

89 microbial cells and biofilms (Davis et al., 2006; Abdel Aal et al., 2010a, 2010b; Albrecht et al.,

90 2011; Revil et al., 2012; Zhang et al., 2013; Mellage et al., 2018; Rosier et al., 2019; Kessouri

91 et al., 2019).

92 Motivated by these successful laboratory measurements (i.e., Abdel Aal and Atekwana, 2014),

93 the IP method has also been used to characterize biogeochemical degradation of contaminants

94 at the field scale (Williams et al., 2009; Slater and Binley 2006; Flores Orozco et al., 2011;

95 2012b; 2013; 2015; Maurya et al., 2017). Natural accumulations of organic matter in areas with

96   indigenous iron-reducing bacteria might result in naturally reduced zones and the precipitation

97   of iron sulfide minerals. Wainwright et al. (2016) demonstrated the applicability of IP imaging

98   to identify naturally reduced zones, i.e., hot spots in floodplains. Moreover, in a recent study,

99   Flores Orozco et al. (2020) demonstrated the possibility to delineate biogeochemically active

100 zones in a municipal solid waste landfill even in the absence of iron sulfides. Flores Orozco et

101 al. (2020) argued that the high content of organic matter itself might explain both, the high

102 polarization response and high rates of microbial activity; thus, opening the possibility to

103 delineate biogeochemical hot spots that are not related to iron-reducing bacteria. This

104 conclusion is consistent with previous studies performed in marsh and peat soils, areas with a

105 high organic matter content and high microbial turnover rates (Mansoor and Slater, 2007;

106 McAnallen et al., 2018). Peat soils are characterized by a high surface charge and have been

107 suggested to enhance the IP response (Slater and Reeve, 2002). Mansoor and Slater (2007)

108 concluded that the IP method is a useful tool to map iron cycling and microbial activity in marsh

109 soils. Uhlemann et al. (2016) found differences in the electrical resistivity of peat according to

110 saturation, microbial activity, and pore water conductivity; however, their study was limited to

111 direct-current resistivity and did not investigate variations in the IP response. In contrast to

112 these observations, laboratory studies have shown a low polarization response in samples with

113 a high organic matter content, despite its high CEC (Schwartz and Furman, 2014). Based on

114 field measurements, McAnallen et al. (2018) found that active peat is less polarizable due to

115 variations in groundwater chemistry imposed by sphagnum mosses; while degrading peat

116 resulted in low resistivity values and a high polarization response. Based on measurements with

117 the Fourier Transform Infrared (FTIR) Spectroscopy in water samples, the authors concluded

118 that the carbon-oxygen (C=O) double-bound in degrading peat correlated with the polarization

119 magnitude of the peat material. Based on laboratory investigations, Ponziani et al. (2011) also

120 conclude that decomposition of peat occurs predominantly by aerobic respiration, i.e. using

121 molecular oxygen as the terminal electron acceptor to oxidize organic matter. Thus

122 decomposition rates are expected to be highest at the interface between the oxic and anoxic

123 zones.

124 Based on these promising previous results, we believe that the IP method is a potentially useful

125 tool for in-situ investigation of biogeochemical processes. However, different lab and field

126 investigations do not offer a clear interpretation scheme of general validity. This study presents

127 an extensive IP imaging dataset collected at a peatland site to investigate the controls on the IP

128 response in biogeochemically active areas. IP monitoring results are compared to geochemical

129 data obtained from freeze cores and pore water sample analysis. Our main objectives are (i) to

130   assess the applicability of the IP method to spatially delimit highly active biogeochemical areas

131   in the peat soil and (ii) to investigate whether the local IP response is related to the accumulation

132   of iron sulfides or high organic matter turnover.

133   **2 Material and methods**

134   2.1 Study site

135   The study site is part of the Lehstenbach catchment located in the Fichtelgebirge mountains

136   (Fig. 1a), a low mountain range in north-eastern Bavaria (Germany) close to the border to the

137   Czech Republic. Various soil types including Dystric Cambisols, Haplic Podsols, and Histosols

138   (i.e. peat soil) cover the catchment area of approximately 4.2 km², situated on-top of variscan

139   granite bedrock (Strohmeier et al., 2013). The catchment is bowl shaped (Fig. 1b), and

140   minerotrophic riparian peatlands have developed around the major streams. The plot scale study

141   site (Fig. 1c) is located in a riparian peatland draining into a nearby stream close to the

142   catchment's outlet (Fig. 1b).

143   The groundwater level in this area annually varies within the top 30 cm of the peat soil and was

144   5-10 cm below the surface during the measurement campaign. The local groundwater flow has

145   a S-SW orientation (Durejka et al., 2019) towards a nearby drainage ditch. Permanently high

146   water saturation of the peat soil favors the development of anoxic biogeochemical processes

147   close to the surface. Frei et al. (2012) demonstrated that hot spots, related to the stimulation of

148   iron reducing bacteria and accumulation of iron sulfides, are generated by small scale

149   subsurface flow processes and the spatial non uniform availability of electron acceptors and

150   donors induced by the peatland's typical micro topography. Transport limited and spatially non

151   uniform availability of electron acceptors and donors, which to a large extent is controlled by

152   subsurface flow patterns induced by the wetland's micro-topography (hummocks and hollows),

153   in combination with labile carbon stocks are the primary drivers in generating biogeochemical

154   hot spots in the peatland (Frei et al., 2012; Mishra and Riley, 2015).

155   2.2 Experimental plot and geochemical measurements

156   The experimental plot for the geophysical measurements covers approximately 160 m² (12.6 x

157   12.6 m, Fig. 1c) of the riparian peatland. Sphagnum Sp. (peat moss) and Molinia caerulea

158   (purple moor-grass) dominate the vegetation, with the sphagnum and purple moor-grass

159   abundance being higher in the Northern part of the plot (Fig. 2a and 2b). In the Southeastern

160   region, where the sphagnum is less abundant, permanent surface runoff was observed (Fig. 2d).

161   To measure the thickness of the peat, a stainless-steel rod (0.5 cm in diameter) was pushed into

162 the ground until it reached the granitic bedrock (similar to Parry et al., 2014). Peat thickness

163 was measured with a 1 m resolution in E-W direction and 0.5 m resolution in N-S direction.

164 During the experiments, the local groundwater level was measured in two piezometers.

165 Groundwater samples were collected at three different locations (S1, S2, and S3 indicated in

166 Fig. 3) using a bailer. Pore water profiles were taken at S1, S2, and S3 at 5 cm intervals to a

167 maximum depth of 50 cm below ground surface (bgs) using stainless steel mini-piezometers.

168 All water samples were filtered through 0.45 µm filters and analyzed for fluoride, chloride,

169 nitrite, bromide, nitrate, phosphate, and sulfate using an ion chromatograph (Compact IC plus

170 882, Metrohm GMBH). Dissolved organic carbon (DOC) was measured using a Shimadsu TOC

171 analyzer via thermal combustion. Dissolved iron species (Fe^{2+}) and total iron (Fe^{tot})

172 concentrations were measured photometrically using the 1,10-phenanthroline method on pore

173 water samples that had been stabilized with 1% vol/vol 1M HCl in the field (Tamura et al.,

174 1974). Two freeze cores (see Fig. 2d) were extracted at locations S1 and S2 (Fig. 3) by pushing

175 an 80-cm long stainless-steel tube into the peat. After the tube was installed, it was filled with

176 a mixture of dry ice and ethanol. After around 20 minutes, the pipe with the frozen peat sample

177 was extracted and stored on dry ice for transportation to the laboratory at the University of

178 Bayreuth. Both freeze cores were cut into 10 cm segments. Each segment was analyzed for

179 reactive iron (1M HCl extraction and measured for Fe^{tot} as described above) (Canfield, 1989),

180 reduced sulfur species using the total reduced inorganic sulfur (TRIS) method (Canfield et al.,

181 1986) and carbon and nitrogen concentrations after combustion using a thermal conductivity

182 detector. Peat samples were also analyzed by FTIR using a Vector 22 FTIR spectrometer

183 (Bruker, Germany) in absorption mode; with subsequent baseline subtraction on KBr pellets

184 (200 mg dried KBr and 2 mg sample). Thirty-two measurements were recorded per sample and

185 averaged from 4.500 to 600 cm^{-1} in a similar manner to Biester et al. (2014).

186 2.3 Non-invasive techniques: induced polarization measurements

187 The induced polarization (IP) imaging method, also known as complex conductivity imaging

188 or electrical impedance tomography, is an extension of the electrical resistivity tomography

189 (ERT) method (e.g., Kemna et al., 2012). As such, it is based on four-electrode measurements,

190 where one pair of electrodes is used to inject a current (current dipole) and a second pair of

191 electrodes is used to measure the resulting electrical potential (potential dipole). Modern

192 devices can measure tens of potential dipoles simultaneously for a given current dipole,

193 permitting the collection of dense data sets within a reasonable measuring time. This provides

194 an imaging framework to gain information about lateral and vertical changes in the electrical

195 properties of the subsurface. IP data can be collected in the frequency domain (FD), where an

196   alternating current is injected into the ground where the polarization of the ground leads to a

197   measurable phase shift between the periodic current and voltage signals. FD measurements can

198   be conducted at different frequencies to gain information about the frequency dependence of

199   the electrical properties of the subsurface. This approach is known as spectral IP (SIP). From

200   the ratio of the magnitudes of the measured voltage and the injected current, as well as the phase

201   shift between the two signals, we can obtain the electrical transfer impedance. The inversion of

202   imaging data sets, i.e. a large set of such four-point transfer-impedance measurements collected

203   at different locations and with different spacing between electrodes along a profile, permits to

204   solve for the spatial distribution of the electrical properties in the subsurface (see deGroot-

205   Hedlin and Constable, 1990; Kemna et al., 2000; Binley and Kemna, 2005).

206   IP imaging results can be expressed in terms of the complex conductivity (σ^*), or its inverse

207   the complex resistivity ($\sigma^*=1/\rho^*$). The complex conductivity can either be denoted in terms of

208   its real (σ') and imaginary (σ'') components, or in terms of its magnitude ($|\sigma|$) and phase (φ):

209    $\sigma^*=\sigma'+i\sigma''=|\sigma|e^{i\varphi}$,   (1)

210   where $i = \sqrt{-1}$ is the imaginary unit, $|\sigma| = \sqrt{\sigma'^2 + \sigma''^2}$ and $\varphi = tan^{-1}\frac{\sigma''}{\sigma'}$.

211   The real part of the complex conductivity is mainly related to the Ohmic conduction, while the

212   imaginary part is mainly related to the polarization of the subsurface. For a more detailed

213   description of the IP method, the reader is referred to the work of Ward (1988), Binley, and

214   Kemna (2005).

215   In this study, we conducted FDIP measurements at 1 Hz along 65 lines during a period of four

216   days in July 2019. We used the DAS-1 instrument manufactured by Multi-Phase Technologies

217   (now MTP-IRIS Inc.). We collected 64 N-S oriented lines (referred to as By 1 to By 64) with

218   20 cm spacing between each line. One additional line (By 68) was collected with a W-E

219   orientation, which intersects the N-S oriented lines at 3 m, as presented in Fig. 3. Each profile

220   consisted of 64 stainless steel electrodes (3 mm diameter) with a separation of 20 cm between

221   each electrode (Fig. 2c). Besides the short electrode spacing, the use of a dipole-dipole

222   configuration with a unit dipole length of 20 cm warranted a high resolution within the upper

223   50 cm of the peat, where the biogeochemical hot spots were expected. We deployed a dipole-

224   dipole skip-0 (i.e., the dipole length for each measurement is equal to the unit spacing of 20

225   cm) configuration, voltage measurements were collected across eight adjacent potential dipoles

226   for each current dipole. The dipole-dipole configuration avoids the use of electrodes for

227   potential measurements previously used for current injections to avoid contamination of the

228   data caused by remnant polarization of electrodes. To evaluate data quality, reciprocal readings

229   were collected along one profile every day (see e.g., LaBrecque et al., 1996; Flores Orozco et
230   al., 2012a; 2019). Reciprocal readings refer to data collected after interchanging current and
231   potential dipoles. We used coaxial cables to connect the electrodes with the measuring device
232   to minimize the distortion of the data due to electromagnetic coupling and cross talking between
233   the cables (e.g., Zimmermann et al., 2008, 2019; Flores Orozco et al., 2013), with the shields
234   of all coaxial cable running together into one ground electrode (for further details see Flores
235   Orozco et al., 2020).

236   3 Results

237   3.1 Data quality and processing

238   In Fig. 4, we present a modified pseudosection showing both normal (negative pseudodepth)
239   and reciprocal (positive pseudodepth) readings in terms of apparent resistivity (ρ_a) and apparent
240   phase (ϕ_a) for the data collected along line By 25. Plots in Fig. 4 show consistency between the
241   normal and reciprocal readings of apparent resistivity (4a) and phase (4b). The principle of
242   reciprocity asserts that normal and reciprocal readings should be the same (e.g., Slater et al.,
243   2000). Hence, the misfit between them can be used to detect outliers, and to quantify data errors
244   (LaBrecque et al., 1996; Flores Orozco et al., 2012a; Slater and Binley, 2006; Slater et al.,
245   2000). Figures 4c and 4d show the histograms of the normal-reciprocal misfits along line By
246   25 for both the resistance and phase (ΔR and $\Delta \phi$ respectively), which exhibit near Gaussian
247   distributions with low standard deviations (as expected for random noise) for both the
248   normalized resistance (S_R=0.027) and the apparent phase (S_ϕ=1.1 mrad). Readings exceeding
249   these standard deviation values were considered as outliers (between 16 and 33% of the data at
250   the different lines) and were removed from the data set prior to the inversion.

251   For the inversion of the IP imaging data set, we used CRTomo, a smoothness-constrained least-
252   squares algorithm by Kemna (2000) that allows inversion of the data to a level of confidence
253   specified by an error model. We used the resistance and phase error models described by Kemna
254   (2000) and Flores Orozco et al. (2012a). The resistance (R) error model is expressed as
255   $s(R)=a+bR$, where a is the absolute error, which dominates at small resistances (i.e., $R < 0$),
256   and b is the relative error, which dominates at high resistance values (LaBrecque et al., 1996;
257   Slater et al., 2000). For the phase, the error model is also expressed as a function of the
258   resistance $s(\phi_a)=cR^d$, where $d<0$ in our study due to the relative low range in the measured
259   resistances (see Flores Orozco et al., 2012a for further details). If $d \rightarrow 0$, the model reduces to

260   the constant-phase-error model (Flores Orozco et al., 2012a) with $s(\phi)=c$ described by Kemna

261   (2000) and Slater and Binley (2006). We quantified the error parameter for each line collected

262   as normal and reciprocal pairs (using the approach outlined by Flores Orozco et al., 2012a) and

263   computed the average value of the error parameters for the inversion of the entire data set. Here,

264   we present inversion results obtained using the error parameters, $a = 0.001\ \Omega$, $b = 2.2\ \%$, and c

265    $= 1$ mrad. For the imaging, we defined a cut-off value of the cumulated sensitivity of $10^{2.75}$,

266   with pixels related to a lower cumulated sensitivity blanked in the images. The cumulated

267   sensitivity values are a widely used parameter to assess the depth of investigation (Kemna et

268   al., 2002; Flores Orozco et al., 2013).

269   **3.2 Complex conductivity imaging results and their link the peat thickness and land**

270   **cover**

271   The thickness of the peat in the plot was found to vary between 40 and 160 cm (Fig. 5). The

272   thickness of the peat unit increased in the W-E direction, with much smaller variations in the

273   N-S direction. Variations in the vegetation cover (as indicated by the three vegetation classes,

274   abundant (*av*), moderate (*mv*) and sparse (*sv*)) do not seem to correspond with the variations in

275   the peat thickness. Note that the N-S orientation of the majority of IP lines is approximately

276   aligned with the direction of minimum changes in the peat thickness.

277   Figure 6 shows the imaging results of the N-S oriented profiles By 25, By 46, and the W-E

278   oriented profile By 68 expressed in terms of the real- (σ') and imaginary (σ") part of the complex

279   conductivity. These images reveal three main electrical units: (i) a shallow unit with high σ'

280   (>5 mSm^{-1}) and high σ" (>80 μSm^{-1}) values in the top 10-20 cm bgs, (ii) an intermediate unit

281   with moderate to low σ' (<5 mSm^{-1}) and moderate σ" (40– 80 μSm^{-1}) values, and (iii) a deep

282   unit characterized by moderate to low σ' (<5 mSm^{-1}) values and the lowest σ" (<40 μSm^{-1})

283   values. The low complex conductivity (both σ' and σ'') in the third unit corresponds to the

284   granite bedrock. The compact structure of the granite, corresponding to low porosity, explains

285   the observed low conductivity values (σ' <5 mSm^{-1}) due to low surface charge and surface area.

286   The second and third unit boundary corresponds to the contact between peat and granite

287   measured using the metal rod (represented by the dashed line in Fig. 5). This shows that the

288   electrical imaging can accurately resolve the contact with the bedrock - even in areas where it

289   is located deeper than 1 m bgs.

290   The shallow and intermediate electrical units are related to the relatively heterogeneous peat

291   (Fig. 6). In the first unit, the electrical images reveal lateral changes along the profiles oriented

292   N-S (By 25 and By 46), while we generally observe higher polarization values (σ") in the

293 northern part of the profiles than in the southern part. This lateral change corresponds to the W-
294 E oriented profile By 68, where the polarization values are the highest around sampling point
295 S1.

296 The phase of the complex conductivity roughly represents the ratio of the polarization (σ'')
297 relative to the Ohmic conduction (σ'). Therefore, it has been argued that the phase represents
298 the polarization effect better than the imaginary conductivity itself as it removes effects
299 stemming from changes in fluid conductivity, saturation, and porosity (Kemna et al., 2004;
300 Ulrich and Slater 2004). Similar to the σ'' images, the phase images presented in Fig. 7 resolve
301 the three main units: (i) the shallow peat unit in the top 10-50 cm is characterized by the highest
302 values ($\phi > 22$ mrad), (ii) the intermediate unit still corresponding to peat, is characterized by
303 moderate ϕ values (between 13 and 22 mrad), and (3) the deep unit, associated to the granitic
304 bedrock, related to the lowest ϕ values (< 13 mrad). The polarization images expressed in terms
305 of ϕ solve the thickness of the peat with higher resolution than the σ' (or σ'') images. Moreover,
306 the shallow unit shows more pronounced lateral variations in the phase than in σ'' and patterns
307 within the peat unit are more clearly defined: Along line By 25, the thickness of the first unit
308 decreases from approx. 0.5 m at 2 m along the profile to 0 m around 10 m at the end of the
309 profile. Along line By 46, the first unit is slightly thicker than 50 cm and shows the highest
310 phase values (~25 mrad) between 0 and 6.5 m along the profile. Beyond 6.5 m, the polarizable
311 unit becomes discontinuous with isolated polarizable (~18 mrad) zones, which also extend to a
312 depth of 50 cm. The geometry of the polarizable shallow unit is consistent with the
313 corresponding results along line By 68, which crosses By 25 and By 46 at 3 m along these lines
314 (S1 and S3 are located at these intersections). In particular, it is clear that the highest phase
315 values were consistently found in the shallowest 50 cm in the peat unit, at the depth where the
316 presence of biogeochemical hot spots has been reported in previous studies (e.g., Frei et al.,
317 2012).

318 The histograms presented in the right column of Fig. 7 show the distribution of the phase values
319 in the images, with a different color for model parameters extracted above and below the contact
320 between the peat and the granite. The histograms highlight that the lowest phase values clearly
321 correspond to the granite bedrock (< 15 mrad), while higher phase values are characteristic for
322 the peat unit.

323 Fig. 8 presents maps of the electrical parameters at different depths aiming at the identification
324 of a possible link to the vegetation cover: abundant-(*av*), moderate- (*mv*) and sparse vegetation
325 (*sv*), observed at the field (Fig. 5). Such maps present the interpolation of values inverted in

326 each profile. Along each profile, a value is obtained through the average of model parameters

327 (conductivity magnitude and phase) within the surface and a depth of 20 cm (shallow maps)

328 and between 100 and 120 cm (for deep maps). The western part of the experimental plot

329 (between 0 and 4 m in X-direction and between 2 and 9 m in Y-direction) corresponds to a

330 shallow depth to the bedrock (a peat thickness of ~ 50-70 cm) and is associated with a high

331 electrical response in the shallow maps (ϕ >17 mrad, σ'>7 mSm^{-1} and σ''>100 μSm^{-1}). In the

332 Northern part of the experimental plot, in the area with abundant vegetation, we observe a

333 higher polarization response for the top 20 cm (ϕ>20 mrad and σ''>80 μSm^{-1}) than the one

334 corresponding to the moderate vegetation located at the southern part. In contrast, the lowest

335 polarization values (ϕ <15 mrad, and σ'' <80 μSm^{-1}) values are related to the area with sparse

336 vegetation. Thus, maps in Fig. 8 suggest that the biogeochemical process controlling the

337 polarization response correlate to the vegetation. On the contrary, the electrical conductivity

338 (σ') reveals only a weak dependence on the vegetation.

339 To support our observation regarding the electrical response and the vegetation, we present in

340 Fig. 8j to 8l the histograms of the electrical parameters extracted at each one of the three

341 vegetation features (abundant, moderate and sparse vegetation). These histograms show, in

342 general, that the location with sparse vegetation, where the water can be seen on the surface,

343 presents the lowest phase values (histogram peak at 13 mrad). Moderate vegetation corresponds

344 with moderate phase values (histogram highest peak at 17 mrad), while the abundant vegetation

345 corresponds with the highest phase values (histogram peak at 20 mrad) in the top 20 cm. The

346 histogram of the three vegetation features in terms of σ' values overlap each other. However,

347 we observe a strong correlation between σ'' and the vegetation, with variations in σ'' permitting

348 to discriminate between areas with a surface cover with abundant and moderate sphagnum and

349 purple moor-grass.

350 ## 3.3 Comparison of electrical and geochemical data

351 The pore-fluid conductivity measured in water samples retrieved from the piezometers show

352 little variations with values ranging between 6.7 and 10.4 mSm^{-1}. The evaluation of the imaging

353 results measured along profiles By 25, By 46, and By 68 were used to guide the selection of

354 locations for the freeze core and sampling of pore water and groundwater. Sampling points S1

355 and S3 were found in the highly polarizable parts of the uppermost peat unit (high σ' and σ''

356 values). In contrast, sampling point S2 is located in an area characterized by particularly low

357 polarization values. Figures 9a-e show the chemical parameters measured in the water samples,

358 specifically chloride (Cl^{-}), phosphate (PO$_4^{3-}$), dissolved organic carbon (DOC), total iron (Fe$_{tot}$

359 $= Fe^{2+} + Fe^{3+}$), and pH; whereas Fig. 9f-j show the chemical parameters measured in the peat

360 samples extracted from the freeze cores, namely, cation exchange capacity (CEC),

361 concentrations of iron sulfid (FeS or FeS_2), total reactive iron (Fe_{tot}), potassium (K^+), and

362 sodium (Na^+). To facilitate the comparison of electrical parameters and geochemical data, Fig.

363 9k-m show the complex conductivity values (σ', σ'' and ϕ) at the sampling points S1, S2 and

364 S3, which were extracted as vertical 1D profiles from the corresponding imaging results.

365 As observed in Fig. 6 and 7, the complex conductivity values (σ', σ'') were highest within the

366 uppermost 10-20 cm and rapidly decreased with depth. Furthermore, the values of ϕ and σ'' in

367 the top 20 cm at S1 and S3 are significantly higher than those at the location S2. High values

368 of ϕ and σ'' at S1 and S3 correspond with high concentrations of DOC, phosphate$^-$, Fe_{tot} in water

369 samples, as well as with high K^+, and Na^+ contents measured in soil materials extracted from

370 the freeze cores. Fig. 9 reveals consistent patterns between geochemical and geophysical

371 parameters: in the first 10 cm bgs close to the sampling points S1 and S3, we observe complex

372 conductivity values (σ' and σ'') as well as chemical parameters, such as DOC, phosphate, Fe_{tot}

373 at least two times higher than those in S2.

374 Figure 10 shows the actual correlations between complex conductivity and Cl^-, DOC and Fe_{tot}

375 concentrations measured in groundwater samples. In Fig. 10, we also provide a simple linear

376 regression analysis to quantify possible correlations. Figure 10 reveals that the phase has a weak

377 to moderate correlation with DOC, Cl^- and Fe_{tot}. The conductivity (σ') shows a slightly stronger

378 correlation with the DOC, the Cl^- and total iron concentration than the polarization (σ''). The

379 highest σ'' values (>100 μSm^{-1}) are related to the highest DOC and total iron concentration.

380 Hence, it is possible to interpret the high phase values as those related to biogeochemical hot

381 spots.

382 Figure 11 shows the FTIR spectroscopy analysis of the freeze core samples. The spectra show

383 the absorbance intensity at different wavenumbers, C-O bond (~1050 cm^{-1}), C=O double-bound

384 (~1640 cm^{-1}), carboxyl (~1720 cm^{-1}) and O-H bonds (~3400 cm^{-1}). The peaks are also indicated

385 in Fig. 11 with the interpretation based on the typical values reported in peatlands, for instance

386 McAnallen et al. (2018) or Artz et al. (2008).

4 DISCUSSION

4.1 Biogeochemical interpretation

389 The geochemical and geoelectrical parameters presented in Fig. 6-7 and 9 displayed consistent

390 patterns, with the highest values within the uppermost 20 cm around S1 and S3. The high DOC,

391   K^+ and phosphate concentrations in the uppermost peat layers and especially in the areas found

392   to be biogeochemically active, strongly suggest that there is rapid decomposition of dead plant

393   material in these areas (Bragazza et al., 2009). Ions such as K^+ and phosphate are essential plant

394   nutrients, and phosphate species especially are often the primary limiting nutrient in peatlands

395   (Hayati and Proctor, 1991). The presence of dissolved phosphate in pore waters suggests that

396   (i) the plant uptake rate of this essential nutrient is exceeded by its production through the

397   decomposition of plant material; and (ii) that organic matter turnover must be rapid indeed to

398   deliver this amount of phosphate to the pore water. This is supported by the DOC concentrations

399   in pore waters exceeding 10 mM. DOC is produced as a decomposition product during

400   microbial hydrolysis and oxidation of solid phase organic carbon via enzymes such as phenol

401   oxidase (Kang et al., 2018). Enzymatic oxidation processes are enhanced by oxygen ingress via

402   diffusion and more importantly by water table fluctuations that work as an 'oxygen pump' to

403   the shallow subsurface (Estop-Aragonés et al., 2012). Thus, an increased DOC concentration

404   in the pore water can be used as an indicator for microbial activity (Elifantz et al., 2011; Liu,

405   2013). The small amount of phosphate measured in the less active area S3 can be explained by

406   adjective transport from the active area S1, which is directly 'up-stream' of S2. In this case,

407   adjective water flow through the uppermost peat layers along the hydrological head gradient

408   may have transported a small amount of reaction products from the biogeochemical source

409   areas to the 'non-active' area. The high DOC, Fe, K^+ and phosphate levels confirm our initial

410   interpretation of the highly conductive and polarizable geophysical units within the first 20 - 50

411   cm bgs in the surroundings of S1 and S3 as biogeochemically active areas.

412   The high DOC concentrations are also likely to be directly or indirectly responsible for the Fe

413   maximum in the upper layers. Dissolved Fe was predominantly found as Fe^{2+} (reducing

414   conditions) suggesting either that high labile DOC levels maintain a low redox potential, or that

415   the dissolved Fe^{2+} was complexed with the DOC limiting the oxidation kinetics enough so that

416   Fe^{2+} can accumulate in peat pore waters. The TRIS analysis clearly showed very low levels of

417   sulfide minerals in both freeze cores, especially in the uppermost peat layers. This was

418   unexpected considering the reducing conditions implied by the dominance of pore water Fe^{2+}.

419   We argue that the lack of sulfide minerals is due to insufficient H_2S or HS^- needed to form FeS

420   or FeS_2, or that the redox potential was not low enough to reduce sulfate to H_2S or HS^-. Both

421   mechanisms are possible, as groundwater in the catchment has generally low sulfate

422   concentrations and sulfate was detected in peat pore water samples, which would not be

423   expected if redox potentials were low enough to reduce sulfate to sulfide. The chemical analyses

424   do not reveal any significant or systemic vertical gradient in mineral sulfide concentrations, as

425   expected for the site (Frei et al., 2012). The maximum in extractable (reactive) solid phase Fe

426   was also located in the upper most peat layer at the 'hot spot' S1. This Fe was likely in the form

427   of iron oxides or bound to/in the plant organic matter. Such iron rich layers typically form at

428   the redox boundary between oxic and anoxic zones and can be quite dynamic depending on

429   variations in the peatland water levels and oxygen ingress (Wang et al., 2017; Estop-Aragonés,

430   2013).

431   Similar to other peatlands, the FTIR spectra show the presence of carbon-oxygen bonds such

432   as C-O, C=O and COOH booth at S1 and S2, furthermore, the peak intensities at S1 tend to

433   decrease with the depth, while the peak intensities at S2 samples tend to increase correlated to

434   the IP response. The phosphate and Fe could potentially form complexes with the O-H groups

435   that show an absorbance peak at 1050 cm^{-1} (Arai and Sparks, 2001; Parikh and Chorover, 2006).

436   Furthermore, the iron can also form complexes with the carboxyl groups (absorbance at ~1720

437   cm^{-1}).

4.2 Correlation between the peat and the electrical signatures

439   The two electrical units observed within the peat indicate variations in the biogeochemical

440   activity with depth. Thus, it is likely that the uppermost unit characterized by the highest σ', σ'',

441   and ϕ values corresponds with an active biogeochemical zone, i.e., a hot spot. Consequently,

442   the second electrical unit associated with moderate σ, σ'', and ϕ values is probably related to a

443   less biogeochemical active or even inactive zone in the peat. The third unit represents the

444   granitic bedrock. The low metal content and the well crystalized form of the granite leads to

445   low σ'' values (here, $< 40\ \mu Sm^{-1}$), as suggested by Marshall and Madden (1959).

446   The high polarization response of the peat is consistent with the measurements of McAnallen

447   et al. (2018), who performed time-domain IP measurements in different peatlands. They suggest

448   that the active peat is less polarizable due to the presence of the abundant sphagnum cover.

449   They found that in the areas where the peat is actively accumulating, the ratio of the vascular

450   plants and the non-vascular sphagnum is low, and therefore, the oxygen availability is low.

451   However, the sphagnum is expected to exude a small amount of carbon into the peat. Fenner et

452   al. (2004) found that the sphagnum contributes to the DOC leachate to the pore water, which is

453   contradictory to the model of McAnallen et al. (2018). Our observations also show that the high

454   DOC content correlates to an abundant sphagnum cover, in agreement with the observations by

455   Fenner et al. (2004), but we cannot clearly tie this to exudates from roots or decomposition of

456   decaying organic matter. Moreover, at our study site the abundant sphagnum grows in

457   conjunction with abundant purple moor-grass. Figures 8-9 reveal an increase in the polarization

458 response (σ'', ϕ) with both the abundant vegetation as well as with DOC concentrations
459 measured in pore water. Thus, supporting our interpretation that high polarization values ($\sigma'' >$
460 100 μSm^{-1} and $\phi >$ 20 mrad) correspond to biogeochemical hot spots rather than vegetation type.
461 Recent studies have demonstrated an increase in the polarization response due to the
462 accumulation of biomass and activity in the root system (e.g., Weigand and Kemna 2017;
463 Tsukanov and Schwartz, 2020). However, the sphagnum does not have roots; on the other hand,
464 the vascular purple moor-grass can contribute to the high IP, as the roots transport oxygen into
465 the deeper area which contributes to the increase in the polarity and normalized chargeability
466 of the peat (McAnallen et al., 2018).

467 ## 4.3 Possible polarization mechanisms

468 The low-frequency polarization response of subsurface materials is usually attributed to either
469 electrode polarization of highly conductive metallic minerals (e.g., Pelton et al., 1978; Wong,
470 1979) or the polarization of the electrical double layer (EDL) covering charged surfaces of
471 electrically non-conducting solid matter (e.g., Waxman and Smits, 1968; Revil and Florsch,
472 2010; Revil, 2012).

473 Electrode polarization arises from the conductivity contrast between the high electronic (or
474 semi-conductor) conductivity of the metallic mineral and the much lower electrolytic
475 conductivity of the surrounding pore fluid (Wong, 1979). This so-called charge polarization has
476 its maximum at relatively high frequencies (>>1 kHz) unless the conducting minerals are large
477 (Bücker et al., 2018). If charge-transfer reactions take place at the mineral-electrolyte interface,
478 e.g., due to the presence of metallic ions in the electrolyte, the charge polarization is
479 accompanied by a concentration polarization, which potentially shifts the maximum of the
480 electrode-polarization response into the low-frequency range (Bücker et al., 2018). The
481 magnitude of electrode polarization is proportional to the volume content of the conductive
482 minerals (Wong, 1979).

483 In this study, we have found a strong correlation between the polarization response (ϕ and σ'')
484 and Fe_{tot} in the solid phase and a less pronounced correlation between the polarization response
485 and the concentration of dissolved iron in the liquid phase (see Fig. 10). If the iron in the solid
486 phase occurred in the form of highly conductive minerals, the two above correlations would
487 clearly point to an electrode-polarization mechanism as a possible explanation for the observed
488 response. Previous studies (e.g., Flores Orozco et al., 2011; 2013) imply that iron sulfides (FeS
489 or FeS_2) in sediments polarize as long as sufficient Fe^{2+} cations are available in the pore water.
490 However, in the case of the present study, the lack of sulfide, and the rather high Eh (inferred

from presence of sulfate) in the pore water, do not favor the precipitation of conductive sulfides such as pyrite. Under these conditions, iron would rather precipitate as iron oxide or form iron-organic matter complexes. The electrical conductivity of most iron oxides is orders of magnitude smaller than the conductivity of sulfides (e.g., Cornell and Schwertmann, 1996), and is thus too low to explain an increased electrode polarization. The only highly conductive iron oxide is magnetite, with a conductivity similar to pyrite (Atekwana et al., 2016). Consequently, the presence of magnetite could explain the electrode polarization. However, the low pH (~5) typical for peat systems does not favor the precipitation of magnetite, but rather less conducting, and thus, less polarizable iron (oxy)hydroxides such as ferrihydrite (Andrade et al., 2010; Linke and Gislason, 2018). As indicated by the FTIR analysis, the iron might furthermore have built complexes with the carboxyl (absorbance at ~1720 cm^{-1}). However, it is not clear if these iron complexes might have a sufficiently high electrical conductivity and - in the fashion of conductive iron minerals - permit electrode polarization mechanism.

In addition to the polarization of conductive minerals, the polarization response can also be caused by the polarization of the electrical double layer (EDL). The EDL consists of an inner Stern layer of cations adsorbed to the charged solid surface and an outer diffuse layer. Together, these two layers screen the (usually) negative charge of the solid surface and represent a highly conductive and, thus, polarizable surface layer. Depending on the specific geometry of solid and liquid phases, EDL polarization can be understood in terms of the polarization of isolated EDL-covered grains (e.g., Schwarz, Schurr, Leroy et al., 2008) or in terms of membrane polarization linked to EDL-covered pore constrictions (e.g., Marshall and Madden, 1959; Bücker and Hördt, 2013; Bücker et al., 2019). Regardless of the specific mechanism, all EDL polarization mechanisms strongly depend on the specific surface area of the material and the charge density at the surface (Revil, 2012; Waxman and Smits, 1968).

The product of both surface charge density and surface area can be quantified by the Cation Exchange Capacity (CEC) of a material. As peat mainly consists of organic matter known to have a high CEC (even compared to most clay minerals; e.g., Schwartz and Furman, 2014; and references therein), EDL polarization of charged organic surfaces may explain the observed IP response. However, in this case, we would expect an increase of the polarization magnitude with the CEC, which we did not observe in our data. The CEC values of the freeze core samples all vary within a narrow range of 5 to 25 meq/kg and we did not observe any correlation between CEC and changes in the polarization magnitude (σ'', ϕ). Ponziani et al. (2011), who conducted SIP measurements on a set of peat samples, have reported a similar observation previously. In summary, the measured CEC is high enough to explain a rise in EDL-polarization; however,

525   the (small) variation in CEC does not explain the observed variation in the polarization

526   magnitude.

527   The pH of the pore fluid is also known to control the magnitude of EDL polarization; an increase

528   of pH usually corresponds with an increase of the polarization magnitude (e.g., Skold et al.,

529   2011). At low pH values, H^+ ions occupy (negative) surface sites and thus reduce the net surface

530   charge of the EDL (e.g., Hördt et al., 2016; and references therein). Our data seems to show the

531   opposite behavior: we found a lower pH in the highly polarizable anomalies at S1 and S3

532   compared to site S2 (the inactive and less polarizable location); while the pH increases at depth

533   for decreasing values in the polarization (both σ'' and ϕ). At the same time, variations in pH are

534   within the range 4.45 and 5.77 and thus might not be sufficiently large to cause the observed

535   variation in the polarization response.

536   Besides pH, pore fluid salinity plays a major role in the control of EDL polarization. Laboratory

537   measurements on sand and sandstone samples indicated that an increase in salinity leads to an

538   early increase of the imaginary conductivity, which is eventually followed by a peak and a

539   decrease at very high salinities during later stages of the experiments (e.g., Revil and Skold,

540   2011; Weller et al., 2015). Hördt et al. (2016) provided a possible theoretical explanation of

541   this behavior: In their membrane-polarization model, salinity controls the thickness of the

542   (diffuse layer) of the EDL and depending on the specific geometry of the pores; there is an

543   optimum thickness, which maximizes the magnitude of the polarization response. In the present

544   study, we observed that an increase in salinity (as indicated by the high Cl^- concentrations

545   within the uppermost 10 cm at all sampling locations) is associated with an increase in the

546   polarization magnitude response (e.g., Revil and Skold, 2011; Weller et al., 2015; Hördt et al.,

547   2016). However, the highest Cl^- concentrations were observed for the shallow layers at location

548   S2, where we measured lower polarization magnitudes (in terms of σ'', ϕ) compared to S1 and

549   S3.

550   The strong correlation between the polarization response and the DOC suggest an, as yet not

551   fully understood, causal relationship. A similar observation has recently been reported by Flores

552   Orozco et al. (2020), who found a strong correlation between DOC as a proxy of microbial

553   activity and both σ' and σ'' in a municipal waste landfill in Austria. McAnallen et al. (2018)

554   reported a strong correlation between the occurrence of long-chained C=O double bonds and

555   the total chargeability of peat material. The upper peat layers are exposed to oxygen leading to

556   oxidation of the peat and formation of C=O double bonds at solid phase surfaces and in the pore

557   water DOC. Such long-chained organic molecules have an increased polarity and thus more

558   readily attach (or even form at organic matter surfaces) to the surface of solid organic and

559   mineral particles (Alonso et al., 2009). Based on a membrane-polarization model, Bücker et al.

560   (2017) predict an increase of the polarization magnitude in the presence of wetting (i.e., long-

561   chained) hydrocarbon in the free phase. The long-chained polar DOC attaches to the peat

562   surface, similar to polar hydrocarbon, and so it might provide extra surface charge, thus

563   reducing the pore space and causing membrane polarization (Marshall and Madden, 1959).

5 Conclusions

565   We investigated the applicability of induced polarization (IP) as a tool to identify and localize

566   biogeochemically active areas or "hot spots" in peatlands. IP imaging results revealed a high

567   polarization response for areas that based on the solid and solution phase chemistry can be

568   interpreted as biogeochemically active. The chemical analysis of the groundwater samples and

569   the freeze core indicate that the top 10-20 cm correspond to the highest geochemical activity,

570   whereas the deeper areas of the peat are less active. Accordingly, only the upper 10-20 cm can

571   be defined as biogeochemical hot spots. Moreover, our geophysical survey shows that IP

572   imaging can delineate the geometry of the hot spot with high spatial resolution. In this regard,

573   indicators for increased biogeochemical activity (DOC, phosphate) correspond to a high IP

574   response (σ'' and phase values).

575   Although the exact polarization mechanism is not fully understood, our results reveal that the

576   IP response of the peat changes with the level of biogeochemical activity. Thus, the IP method

577   is capable of distinguishing between biogeochemical active and inactive zones within the peat.

578   The phase values show a contrast between these active and inactive zones and characterize the

579   geometry of the hot spots even if iron sulfides are not present. Previous studies have only

580   investigated the conductive properties of the peat; however, biogeochemical activity within the

581   peat has not been investigated. In this regard, our study shows a new alternative method to

582   characterize biogeochemical changes and their geometry within the peat with high resolution.

583   For further improvement and understanding of the effect of the organic matter such as DOC or

584   phosphate on the polarization response, further laboratory studies on peat samples with different

585   concentration and mixture of DOC, phosphate and iron in the pore fluid are required.

Acknowledgements

587   This research was supported by the German Research Foundation (DFG) Project FR 2858/2-1-

588   3013594 and GI 792/2-1. The work of Timea Katona was supported by the ExploGRAF project

589   (Development of geophysical methods for the exploration of graphite ores) funded by the
590   Austrian Federal Ministry of Science, Research and Economy.

Data availability

592   All data are available from the corresponding author upon request.

Competing interests.

594   The authors declare that they have no conflict of interest.

Author contribution

596   AFO and TK designed the experimental set-up, TK conducted the field survey and analysis of
597   the geophysical data. BG and SF conducted the geochemical measurements and their
598   interpretation. AFO, MB and TK interpreted the geophysical signatures. TK lead the
599   preparation of the draft, where SF, BG, MB and AFO contributed equally.

600
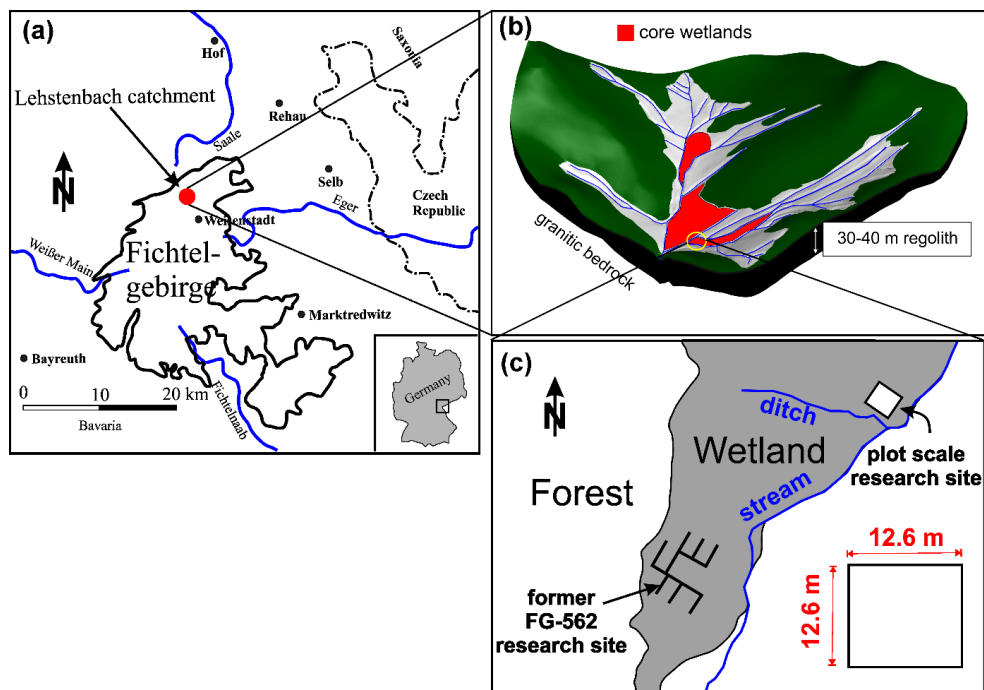
601

Figure 1: (a) General overview of the experimental plot located in the Fichtel Mountains and (b) structure of the bowl shaped Lehstenbach catchment, and (c) location of the experimental plot.

602

603
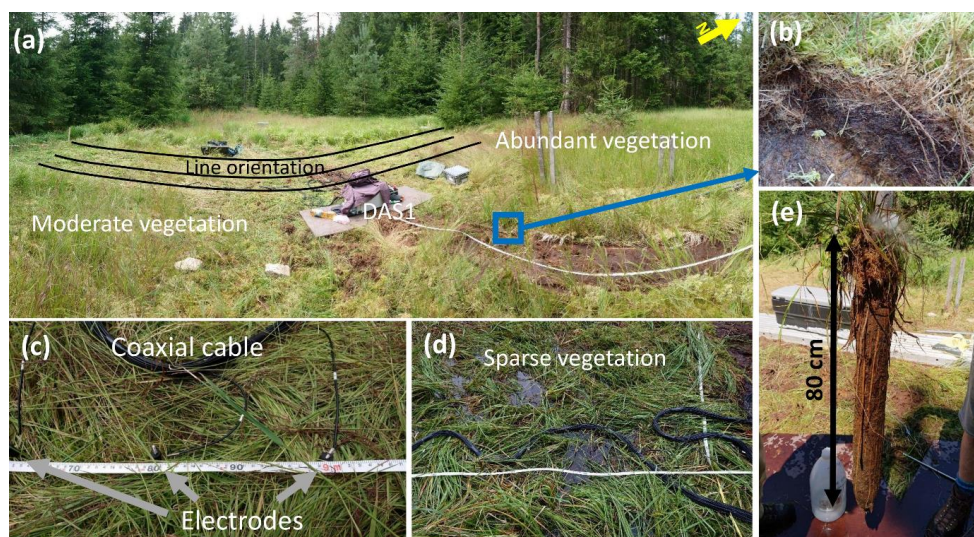
Figure 2: (a) Panoramic overview of the study site and the measurement setup. Pictures show the experimental setup and differences in the vegetation density between the northern and southern part of the experimental plot. The spectral induced polarization (SIP) lines appear distorted due to the panoramic view. (b) Sphagnum in the northern part of the experimental plot. (c) Coaxial cables and stainless steel electrodes used for SIP measurements. (d) Vegetation and the coaxial cable bundle used for IP measurements at the water covered area in the southeastern part of the experimental plot. (e) The freeze core shows the internal structure of the peat.

604
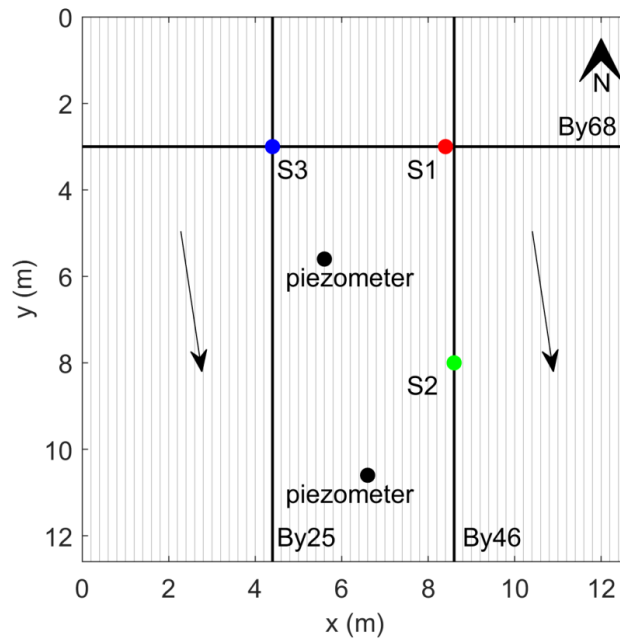
605

Figure 3: Schematic map of the experimental plot. The solid lines represent the measured profiles; the bold lines represent the position of the profiles discussed in this manuscript (By 25, By 46 and By 68). The arrows indicate the ground water flow direction. The points represent the locations of fluid (S1, S2 and S3) and freeze core (S1, S2) samples as well as the position of piezometric tubes, where the water level was measured.

606
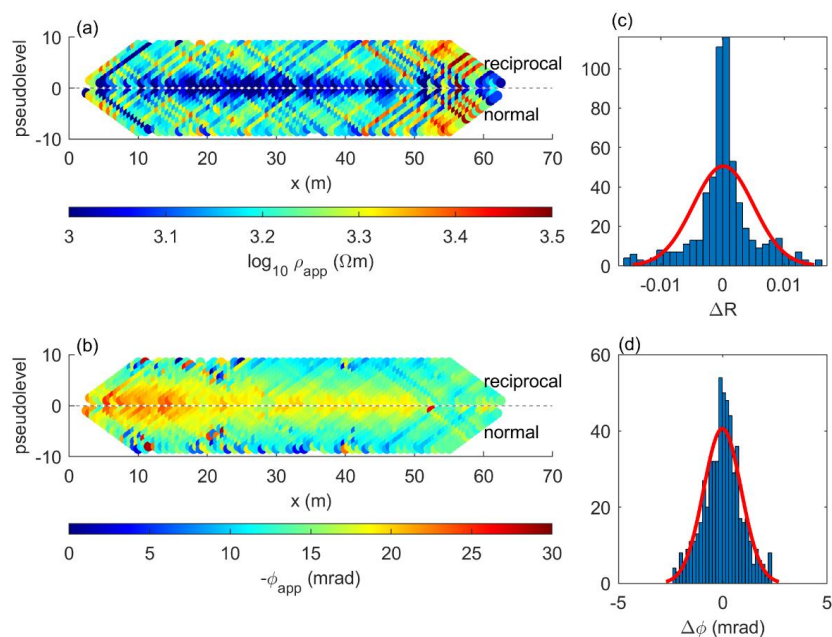
607

Figure 4: Raw data analysis. Raw-data pseudosections of (a) the apparent resistivity and (b) the apparent phase shift for measurements collected along profile By 25. Histograms of the normal-reciprocal misfits of (c) the measured resistance and (d) the apparent phase shift.
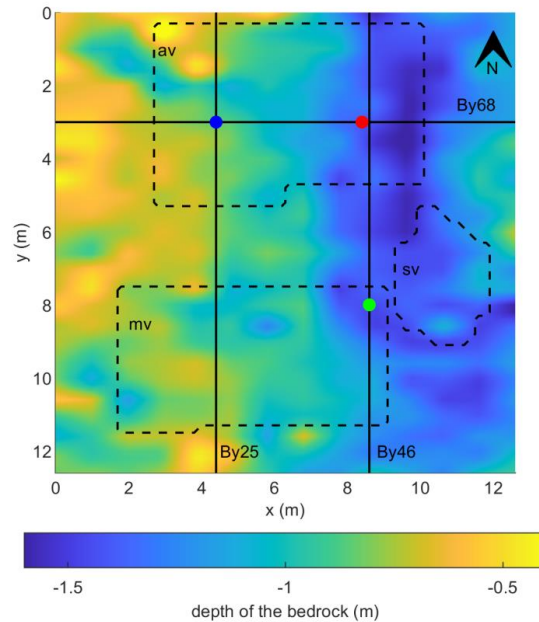
608

Figure 5: Variations in the thickness of the peat layer, i.e., depth to the granite bedrock. The positions of the three selected IP profiles By 25, By 46, and By 68 are indicated (solid lines) as well as the position of the sampling points and the geometry of the three classes of vegetation cover: abundant vegetation (av), moderate vegetation (mv), and sparse vegetation (sv).
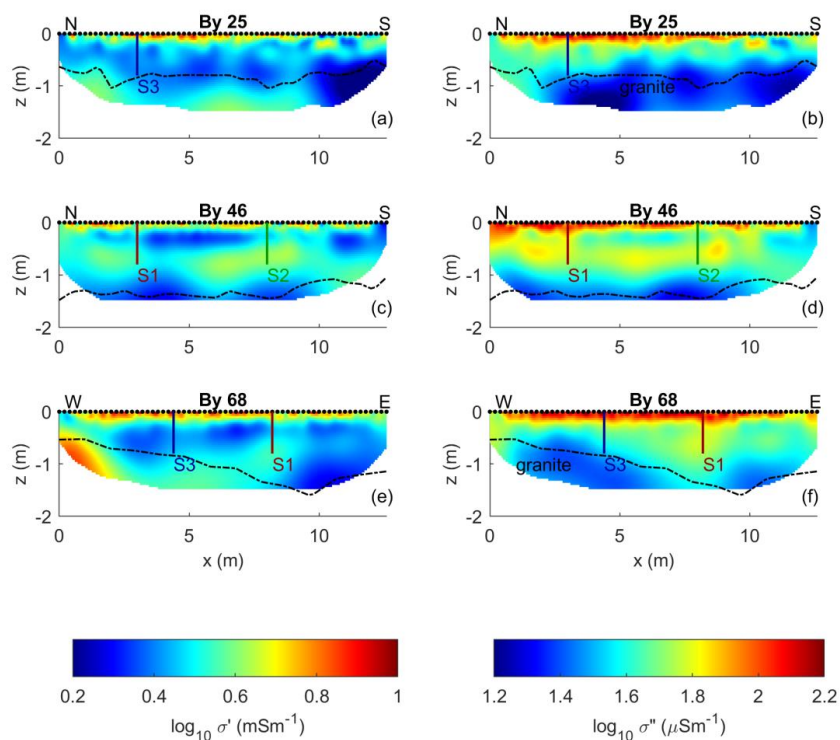
609

Figure 6: Imaging results for data collected along profiles By 25 (a-b), By 46 (c-d), and By 68 (e-f) expressed as real σ' and imaginary σ'' component of the complex conductivity. The dashed lines represent the contact between the peat and granite; the black dots show the electrode positions at the surface. The vertical lines represent the location of the fluid (S1, S2 and S3) and freeze core (S1, S2) samples.
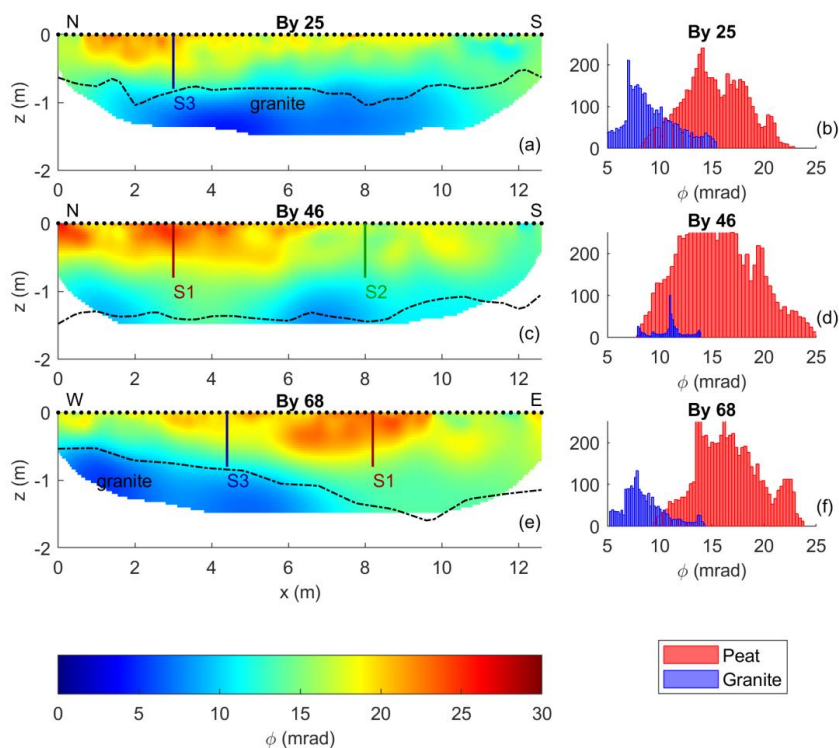
610

Figure 7: Imaging results for data collected along profiles By 25 (a), By 46 (c), and By 68 (e), expressed as phase values φ of the complex conductivity. The dashed lines represent the contact between peat and granite; the black dots show the electrode positions at the surface. The vertical lines represent the location of the fluid (S1, S2, S3) and freeze core (S1, S2) samples. The histograms represent the phase values of the granite and peat extracted from the imaging results in (6b, 6d, 6f) according to the geometry of the dashed lines.
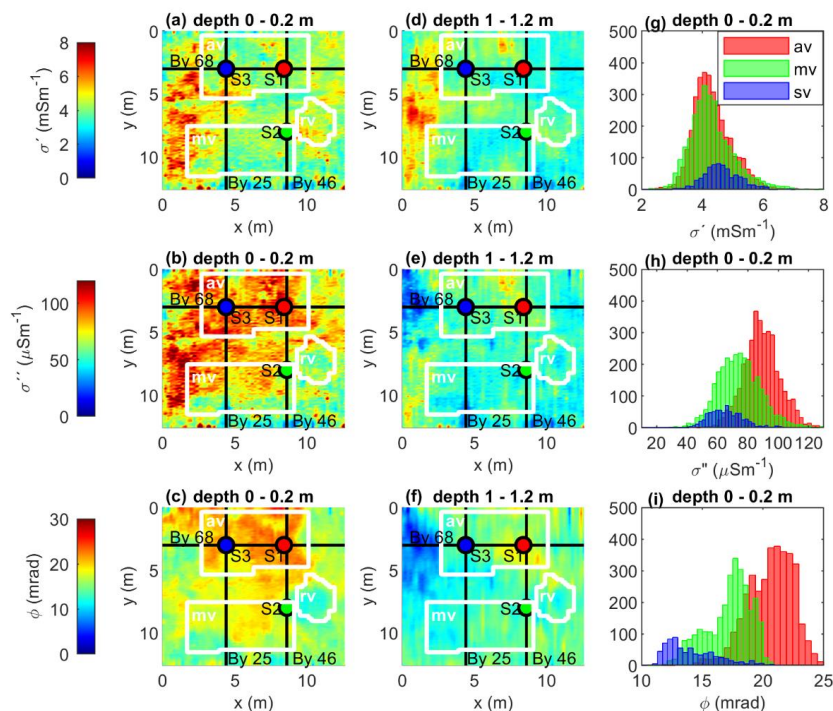
611

Figure 8: Maps of the complex conductivity at different depths. The black lines indicate the profiles By 25, By 46, and By 68. The dots represent the locations of the vertical sampling profiles S1, S2, and S3. The white lines outline areas classified as (av) abundant vegetation, (mv) moderate vegetation, (sv) sparse vegetation, and histograms of the complex-conductivity imaging results of the masked areas, the abundant vegetation (red bins), the moderate vegetation (green bins) and the sparse vegetation (blue bins).

612
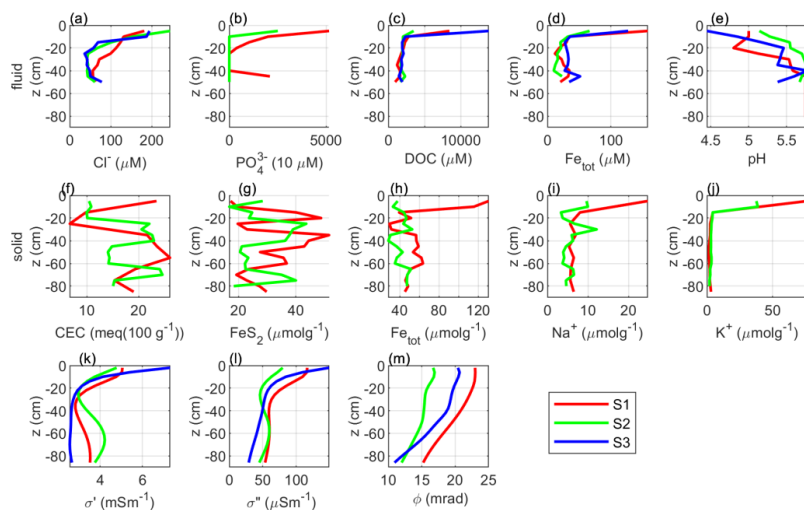
Figure 9: Results of geochemical analyses of water and soil samples. Fluid-sample analysis of the (a) chloride Cl^-, (b) phosphate PO_4^{3-}, (c) dissolved organic carbon, (d) total iron Fe_{tot}, and (e) pH. Freeze-core sample analysis of the (f) cation exchange capacity CEC, (g) iron sulfide FeS_2, (h) total iron Fe_{tot}, (i) sodium Na^+, and (j) potassium K^+. Imaging results at the three sampling locations in terms of (k) real component σ', (l) imaginary component σ'', and (m) phase ϕ of the complex conductivity.

613
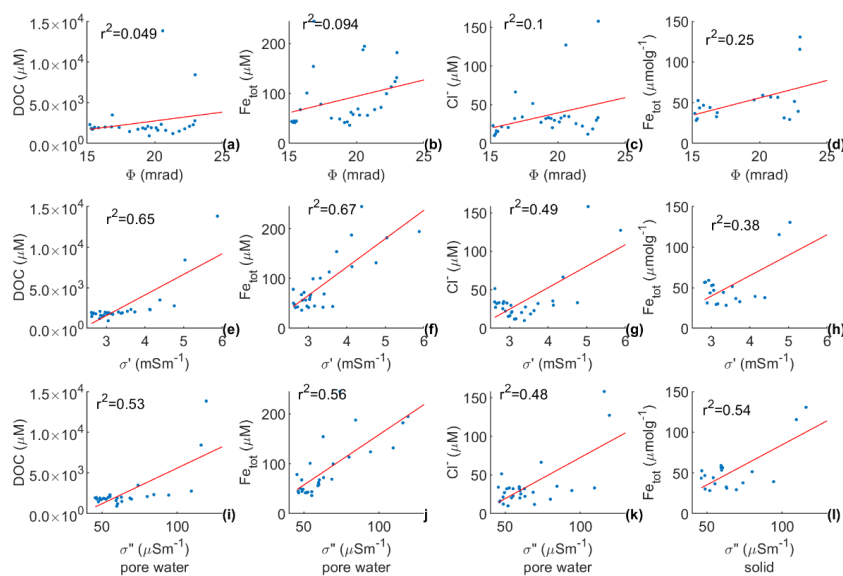
614

Figure 10: Correlations between the geophysical and geochemical parameters, phase (ϕ), the real (σ') and imaginary (σ'') component of the complex conductivity (retrieved from the imaging results) and the biogeochemical analysis, expressed in terms of the dissolved organic carbon (DOC), and chloride (Cl^-) content from the pore fluid samples and total iron (Fe_{tot}) content from pore fluid in $\mu moll^{-1}$ and solid samples in $\mu molg^{-1}$. The correlation coefficients of least square regressions analysis are shown in the top left corners of the subplots.

615
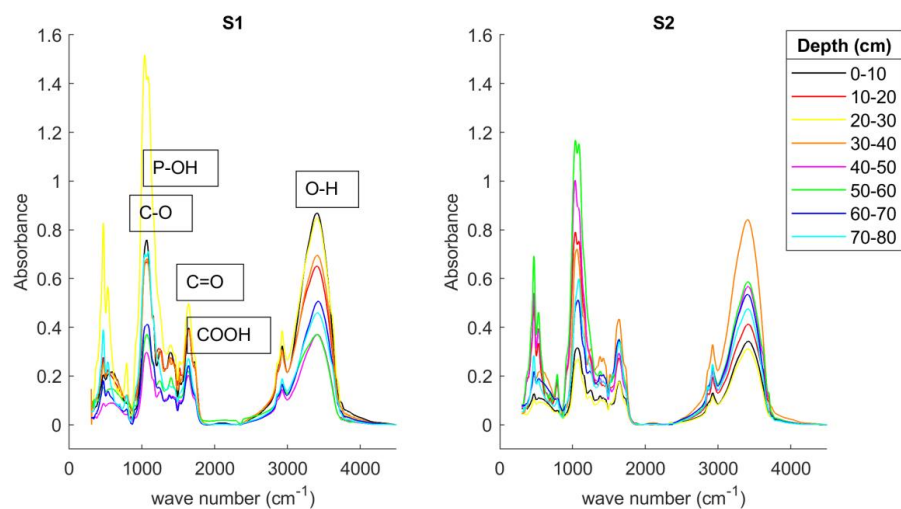
Figure 11: Fourier transform infrared (FTIR) spectroscopy of the freeze core samples collected at S1 (left panel) and S2 (right panel). Each sample was extracted from the 10 cm segments. The lines represent the depth at every 10 cm between 0 and 80 cm below ground surface. The relevant peaks show the absorbance intensity, the interpretation is based on Artz et al. (2008), Arai and Sparks (2001), Parikh and Chorover (2006).

References

1. Abdel Aal, G. Z., & Atekwana, E. A. (2014). Spectral induced polarization (SIP) response of biodegraded oil in porous media. *Geophysical Journal International*, *196*(2), 804-817.

2. Abdel Aal, G. Z., Atekwana, E. A., Rossbach, S., & Werkema, D. D. (2010a). Sensitivity of geoelectrical measurements to the presence of bacteria in porous media. *Journal of Geophysical Research: Biogeosciences*, *115*(G3).

3. Abdel Aal, Gamal Z., Estella A. Atekwana, and Eliot A. Atekwana. "Effect of bioclogging in porous media on complex conductivity signatures." *Journal of Geophysical Research: Biogeosciences* 115, no. G3 (2010b).

631 4. Abdel Aal, G. Z., Atekwana, E. A., & Revil, A. (2014). Geophysical signatures of
632   disseminated iron minerals: A proxy for understanding subsurface biophysicochemical
633   processes. *Journal of Geophysical Research: Biogeosciences*, *119*(9), 1831-1849.
634

635 5. Albrecht, R., Gourry, J. C., Simonnot, M. O., & Leyval, C. (2011). Complex
636   conductivity response to microbial growth and biofilm formation on phenanthrene
637   spiked medium. *Journal of Applied Geophysics*, *75*(3), 558-564.
638

639 6. Alonso, D. M., Granados, M. L., Mariscal, R., & Douhal, A. (2009). Polarity of the acid
640   chain of esters and transesterification activity of acid catalysts. *Journal of Catalysis*,
641   *262*(1), 18-26.
642

643 7. Andrade, Â. L., Souza, D. M., Pereira, M. C., Fabris, J. D., & Domingues, R. Z. (2010).
644   pH effect on the synthesis of magnetite nanoparticles by the chemical reduction-
645   precipitation method. *Quimica Nova*, *33*(3), 524-527.
646

647 8. Arai, Y., & Sparks, D. L. (2001). ATR–FTIR spectroscopic investigation on
648   phosphate adsorption mechanisms at the ferrihydrite–water interface. *Journal of
649   Colloid and Interface Science*, *241*(2), 317-326.
650

651 9. Artz, R. R., Chapman, S. J., Robertson, A. J., Potts, J. M., Laggoun-Défarge, F., Gogo,
652   S., ... & Francez, A. J. (2008). FTIR spectroscopy can be used as a screening tool for
653   organic matter quality in regenerating cutover peatlands. *Soil Biology and
654   Biochemistry*, *40*(2), 515-527.
655

656 10. Atekwana, E., Patrauchan, M., & Revil, A. (2016). *Induced Polarization Signature of
657   Biofilms in Porous Media: From Laboratory Experiments to Theoretical Developments
658   and Validation* (No. DOE-Okstate-SC0007118). Oklahoma State Univ., Stillwater, OK
659   (United States).
660

661 11. Atekwana, E. A., & Slater, L. D. (2009). Biogeophysics: A new frontier in Earth science
662   research. *Reviews of Geophysics*, *47*(4).
663

664   12. Biester, H., Knorr, K. H., Schellekens, J., Basler, A., & Hermanns, Y. M. (2014).
665   Comparison of different methods to determine the degree of peat decomposition in
666   peat bogs. *Biogeosciences*, *11*(10), 2691-2707.
667

668   13. Binley, A., & Kemna, A. (2005). DC resistivity and induced polarization methods. In
669   *Hydrogeophysics* (pp. 129-156). Springer, Dordrecht.
670

671   14. Binley, A., Hubbard, S. S., Huisman, J. A., Revil, A., Robinson, D. A., Singha, K., &
672   Slater, L. D. (2015). The emergence of hydrogeophysics for improved understanding of
673   subsurface processes over multiple scales. *Water resources research*, *51*(6), 3837-3866.
674

675   15. Boano, F., Harvey, J. W., Marion, A., Packman, A. I., Revelli, R., Ridolfi, L., &
676   Wörman, A. (2014). Hyporheic flow and transport processes: Mechanisms, models, and
677   biogeochemical implications. *Reviews of Geophysics*, *52*(4), 603-679.

678   16. Bragazza, L., Buttler, A., Siegenthaler, A., & Mitchell, E. A. (2009). Plant litter
679   decomposition and nutrient release in peatlands. *Geoph. Monog. Series*, *184*, 99-110.
680

681   17. Bücker, M., & Hördt, A. (2013). Analytical modelling of membrane polarization with
682   explicit parametrization of pore radii and the electrical double layer. *Geophysical
683   Journal International*, *194*(2), 804-813.
684

685   18. Bücker, M., Orozco, A. F., Hördt, A., & Kemna, A. (2017). An analytical membrane-
686   polarization model to predict the complex conductivity signature of immiscible liquid
687   hydrocarbon contaminants. *Near Surface Geophysics*, *15*(6), 547-562.
688

689   19. Bücker, M., Orozco, A. F., & Kemna, A. (2018). Electrochemical polarization around
690   metallic particles—Part 1: The role of diffuse-layer and volume-diffusion relaxation.
691   *Geophysics*, *83*(4), E203-E217.
692

693   20. Bücker, M., Undorf, S., Flores Orozco, A., & Kemna, A. (2019). Electrochemical
694   polarization around metallic particles—Part 2: The role of diffuse surface charge.
695   *Geophysics*, *84*(2), E57-E73.
696

697   21. Canfield, D. E. (1989). Reactive iron in marine sediments. *Geochimica et*
698   *Cosmochimica Acta*, *53*(3), 619-632.

699

700   22. Canfield, D. E., Raiswell, R., Westrich, J. T., Reaves, C. M., & Berner, R. A. (1986).
701   The use of chromium reduction in the analysis of reduced inorganic sulfur in
702   sediments and shales. *Chemical geology*, *54*(1-2), 149-155.

703

704   23. Capps, K. A., & Flecker, A. S. (2013). Invasive fishes generate biogeochemical hotspots
705   in a nutrient-limited system. *PLoS One*, *8*(1), e54093.

706

707   24. Cirmo, C. P., & McDonnell, J. J. (1997). Linking the hydrologic and biogeochemical
708   controls of nitrogen transport in near-stream zones of temperate-forested catchments: a
709   review. *Journal of Hydrology*, *199*(1-2), 88-120.

710

711   25. Cornell, R. M., & Schwertmann, U. (1996). The Iron Oxides, VCH.

712

713   26. Costanza, R., d'Arge, R., De Groot, R., Farber, S., Grasso, M., Hannon, B., ... & Raskin,
714   R. G. (1997). The value of the world's ecosystem services and natural capital. *nature*,
715   *387*(6630), 253-260.

716

717   27. Costanza, R., De Groot, R., Braat, L., Kubiszewski, I., Fioramonti, L., Sutton, P., ... &
718   Grasso, M. (2017). Twenty years of ecosystem services: how far have we come and
719   how far do we still need to go?. *Ecosystem services*, *28*, 1-16.

720

721   28. Davis, C. A., Atekwana, E., Atekwana, E., Slater, L. D., Rossbach, S., & Mormile, M.
722   R. (2006). Microbial growth and biofilm formation in geologic media is detected with
723   complex conductivity measurements. *Geophysical Research Letters*, *33*(18).

724

725   29. Diamond, J. S., McLaughlin, D. L., Slesak, R. A., & Stovall, A. (2020).
726   Microtopography is a fundamental organizing structure of vegetation and soil chemistry
727   in black ash wetlands.

728

729   30. Durejka, S., Gilfedder, B. S., & Frei, S. (2019). A method for long-term high resolution
730   222Radon measurements using a new hydrophobic capillary membrane system. *Journal*
731   *of environmental radioactivity*, *208*, 105980.
732

733   31. Elifantz, H., Kautsky, L., Mor-Yosef, M., Tarchitzky, J., Bar-Tal, A., Chen, Y., & Minz,
734   D. (2011). Microbial activity and organic matter dynamics during 4 years of irrigation
735   with treated wastewater. *Microbial ecology*, *62*(4), 973-981.
736

737   32. Estop-Aragonés, C., Knorr, K. H., & Blodau, C. (2012). Controls on in situ oxygen
738   and dissolved inorganic carbon dynamics in peats of a temperate fen. *Journal of*
739   *Geophysical Research: Biogeosciences*, *117*(G2).
740

741   33. Estop-Aragonés, C., Knorr, K. H., & Blodau, C. (2013). Belowground in situ redox
742   dynamics and methanogenesis recovery in a degraded fen during dry-wet cycles and
743   flooding. *Biogeosciences*, *10*(1), 421-436.
744

745   34. Fenner, N., Ostle, N., Freeman, C., Sleep, D., & Reynolds, B. (2004). Peatland carbon
746   efflux partitioning reveals that Sphagnum photosynthate contributes to the DOC pool.
747   *Plant and Soil*, *259*(1-2), 345-354.
748

749   35. Flores Orozco, A., Williams, K.H., Long, P.E., Hubbard, S.S. and Kemna, A., 2011.
750   Using complex resistivity imaging to infer biogeochemical processes associated with
751   bioremediation of an uranium-contaminated aquifer. *Journal of Geophysical Research:*
752   *Biogeosciences*, *116*(G3).
753

754   36. Flores Orozco, A., Kemna, A., & Zimmermann, E. (2012a). Data error quantification in
755   spectral induced polarization imaging. *Geophysics*, *77*(3), E227-E237.
756

757   37. Flores Orozco, A., Kemna, A., Oberdörster, C., Zschornack, L., Leven, C., Dietrich, P.,
758   & Weiss, H. (2012b). Delineation of subsurface hydrocarbon contamination at a former
759   hydrogenation plant using spectral induced polarization imaging. *Journal of*
760   *contaminant hydrology*, *136*, 131-144.
761

762   38. Flores Orozco, A., Williams, K. H., & Kemna, A. (2013). Time-lapse spectral induced
763   polarization imaging of stimulated uranium bioremediation. *Near Surface Geophysics*,
764   *11*(5), 531-544.

766   39. Flores Orozco, A., Velimirovic, M., Tosco, T., Kemna, A., Sapion, H., Klaas, N., ... &
767   Bastiaens, L. (2015). Monitoring the injection of microscale zerovalent iron particles
768   for groundwater remediation by means of complex electrical conductivity imaging.
769   *Environmental Science & Technology*, *49*(9), 5593-5600.

771   40. Flores Orozco, A., Kemna, A., Binley, A., & Cassiani, G. (2019). Analysis of time-
772   lapse data error in complex conductivity imaging to alleviate anthropogenic noise for
773   site characterization. *Geophysics*, *84*(2), B181-B193.

775   41. Flores Orozco, A., Gallistl, J., Steiner, M., Brandstätter, C., & Fellner, J. (2020).
776   Mapping biogeochemically active zones in landfills with induced polarization imaging:
777   The Heferlbach landfill. *Waste Management*, *107*, 121-132.

779   42. Frei, S., Lischeid, G., & Fleckenstein, J. H. (2010). Effects of micro-topography on
780   surface–subsurface exchange and runoff generation in a virtual riparian wetland—A
781   modeling study. *Advances in Water Resources*, *33*(11), 1388-1401.

783   43. Frei, S., Knorr, K. H., Peiffer, S., & Fleckenstein, J. H. (2012). Surface micro-
784   topography causes hot spots of biogeochemical activity in wetland systems: A virtual
785   modeling experiment. *Journal of Geophysical Research: Biogeosciences*, *117*(G4).

787   44. deGroot-Hedlin, C., & Constable, S. (1990). Occam's inversion to generate smooth,
788   two-dimensional models from magnetotelluric data. *Geophysics*, *55*(12), 1613-1624.

790   45. Gu, B., Liang, L., Dickey, M. J., Yin, X., & Dai, S. (1998). Reductive precipitation of
791   uranium (VI) by zero-valent iron. *Environmental Science & Technology*, *32*(21), 3366-
792   3373.

794   46. Gutknecht, J. L., Goodman, R. M., & Balser, T. C. (2006). Linking soil process and
795   microbial ecology in freshwater wetland ecosystems. *Plant and Soil*, *289*(1-2), 17-34.

796

797   47. Hansen, D. J., McGuire, J. T., Mohanty, B. P., & Ziegler, B. A. (2014). Evidence of

798   aqueous iron sulfid clusters in the vadose zone. *Vadose Zone Journal*, *13*(3), 1-12.

799

800   48. Hartley, A. E., & Schlesinger, W. H. (2000). Environmental controls on nitric oxide

801   emission from northern Chihuahuan desert soils. *Biogeochemistry*, *50*(3), 279-300.

802

803   49. Hayati, A. A., & Proctor, M. C. F. (1991). Limiting nutrients in acid-mire vegetation:

804   peat and plant analyses and experiments on plant responses to added nutrients. *The*

805   *Journal of Ecology*, 75-95.

806

807   50. Hördt, A., Bairlein, K., Bielefeld, A., Bücker, M., Kuhn, E., Nordsiek, S. and Stebner,

808   H., 2016. The dependence of induced polarization on fluid salinity and pH, studied with

809   an extended model of membrane polarization. *Journal of Applied Geophysics*, *135*,

810   pp.408-417.

811

812   51. Kang, H., Kwon, M. J., Kim, S., Lee, S., Jones, T. G., Johncock, A. C., ... & Freeman,

813   C. (2018). Biologically driven DOC release from peatlands during recovery from

814   acidification. *Nature communications*, *9*(1), 1-7.

815

816   52. Kayranli, B., Scholz, M., Mustafa, A., & Hedmark, Å. (2010). Carbon storage and

817   fluxes within freshwater wetlands: a critical review. *Wetlands*, *30*(1), 111-124.

818

819   53. Kemna, A., 2000. Tomographic Inversion of Complex Resistivity: Theory and

820   Application.Der Andere Verlag Osnabrück, Germany

821

822

823   54. Kemna, A., Binley, A., Ramirez, A., & Daily, W. (2000). Complex resistivity

824   tomography for environmental applications. *Chemical Engineering Journal*, *77*(1-2),

825   11-18.

826

827   55. Kemna, A., Vanderborght, J., Kulessa, B., & Vereecken, H. (2002). Imaging and

828   characterisation of subsurface solute transport using electrical resistivity tomography

829   (ERT) and equivalent transport models. *Journal of Hydrology*, *267*(3-4), 125-146.

830

56. Kemna, A., Binley, A., & Slater, L. (2004). Crosshole IP imaging for engineering and
    environmental applications. *Geophysics*, *69*(1), 97-107.

57. Kemna, A., Binley, A., Cassiani, G., Niederleithinger, E., Revil, A., Slater, L., ... &
    Kruschwitz, S. (2012). An overview of the spectral induced polarization method for
    near-surface applications. *Near Surface Geophysics*, *10*(6), 453-468.

58. Kessouri, P., Furman, A., Huisman, J. A., Martin, T., Mellage, A., Ntarlagiannis, D., ...
    & Kemna, A. (2019). Induced polarization applied to biogeophysics: recent advances
    and future prospects. *Near Surface Geophysics*, *17*(6-Recent Developments in Induced
    Polarization), 595-621.

59. LaBrecque, D. J., Miletto, M., Daily, W., Ramirez, A., & Owen, E. (1996). The effects
    of noise on Occam's inversion of resistivity tomography data. *Geophysics*, *61*(2), 538-
    548.

60. Leroy, P., Revil, A., Kemna, A., Cosenza, P., & Ghorbani, A. (2008). Complex
    conductivity of water-saturated packs of glass beads. *Journal of colloid and interface
    science*, *321*(1), 103-117.

61. Linke, T., & Gislason, S. R. (2018). Stability of iron minerals in Icelandic peat areas
    and transport of heavy metals and nutrients across oxidation and salinity gradients–a
    modelling approach. *Energy Procedia*, *146*, 30-37.

62. Liu, H. (2013). Thermal response of soil microbial respiration is positively associated
    with labile carbon content and soil microbial activity. *Geoderma*, *193*, 275-281.

63. Mansoor, N., & Slater, L. (2007). On the relationship between iron concentration and
    induced polarization in marsh soils. *Geophysics*, *72*(1), A1-A5.

64. Marshall, D. J., & Madden, T. R. (1959). Induced polarization, a study of its causes.
    Geophysics, *24*(4), 790-816.

863

864   65. Maurya, P. K., Rønde, V. K., Fiandaca, G., Balbarini, N., Auken, E., Bjerg, P. L., &
865   Christiansen, A. V. (2017). Detailed landfill leachate plume mapping using 2D and 3D
866   electrical resistivity tomography-with correlation to ionic strength measured in screens.
867   *Journal of Applied Geophysics*, *138*, 1-8.

869   66. McAnallen, L., Doherty, R., Donohue, S., Kirmizakis, P., & Mendonça, C. (2018).
870   Combined use of geophysical and geochemical methods to assess areas of active,
871   degrading and restored blanket bog. *Science of the Total Environment*, *621*, 762-771.

873   67. McClain, M. E., Boyer, E. W., Dent, C. L., Gergel, S. E., Grimm, N. B., Groffman, P.
874   M., ... & McDowell, W. H. (2003). Biogeochemical hot spots and hot moments at the
875   interface of terrestrial and aquatic ecosystems. *Ecosystems*, 301-312.

877   68. Mellage, A., Smeaton, C. M., Furman, A., Atekwana, E. A., Rezanezhad, F., & Van
878   Cappellen, P. (2018). Linking spectral induced polarization (SIP) and subsurface
879   microbial processes: Results from sand column incubation experiments. *Environmental*
880   *science & technology*, *52*(4), 2081-2090.

882   69. Mishra, U., & Riley, W. J. (2015). Scaling impacts on environmental controls and
883   spatial heterogeneity of soil organic carbon stocks. *Biogeosciences Discussions*
884   *(Online)*, *12*(2).

886   70. Morse, J. L., Werner, S. F., Gillin, C. P., Goodale, C. L., Bailey, S. W., McGuire, K. J.,
887   & Groffman, P. M. (2014). Searching for biogeochemical hot spots in three dimensions:
888   Soil C and N cycling in hydropedologic settings in a northern hardwood forest. *Journal*
889   *of Geophysical Research: Biogeosciences*, *119*(8), 1596-1607.

891   71. Ntarlagiannis, D., Williams, K. H., Slater, L., & Hubbard, S. (2005). Low-frequency
892   electrical response to microbial induced sulfid precipitation. *Journal of Geophysical*
893   *Research: Biogeosciences*, *110*(G2).

895   72. Ntarlagiannis, D., Doherty, R. and Williams, K.H., 2010. Spectral induced polarization
896   signatures of abiotic FeS precipitation SIP signatures of FeS precipitation. *Geophysics*,
897   *75*(4), pp.F127-F133.

898

899   73. Parikh, S. J., & Chorover, J. (2006). ATR-FTIR spectroscopy reveals bond formation
900   during bacterial adhesion to iron oxide. *Langmuir*, *22*(20), 8492-8500.

901

902   74. Parry, L. E., West, L. J., Holden, J., & Chapman, P. J. (2014). Evaluating approaches
903   for estimating peat depth. *Journal of Geophysical Research: Biogeosciences*, *119*(4),
904   567-576.

905

906   75. Pelton, W. H., Ward, S. H., Hallof, P. G., Sill, W. R., & Nelson, P. H. (1978). Mineral
907   discrimination and removal of inductive coupling with multifrequency IP. *Geophysics*,
908   *43*(3), 588-609.

909

910   76. Personna, Y. R., Ntarlagiannis, D., Slater, L., Yee, N., O'Brien, M., & Hubbard, S.
911   (2008). Spectral induced polarization and electrodic potential monitoring of microbially
912   mediated iron sulfid transformations. *Journal of Geophysical Research: Biogeosciences*,
913   *113*(G2).

914

915   77. Placencia-Gómez, E., Slater, L., Ntarlagiannis, D., & Binley, A. (2013). Laboratory SIP
916   signatures associated with oxidation of disseminated metal sulfids. *Journal of
917   Contaminant Hydrology*, *148*, 25-38.

918

919   78. Ponziani, M., Slob, E. C., Ngan-Tillard, D. J. M., & Vanhala, H. (2011). Influence of
920   water content on the electrical conductivity of peat. *International Water Technology
921   Journal*, *1*(1), 14-21.

922

923   79. Revil, A. (2012). Spectral induced polarization of shaly sands: Influence of the electrical
924   double layer. *Water Resources Research*, *48*(2).

925

926   80. Revil, A., & Florsch, N. (2010). Determination of permeability from spectral induced
927   polarization in granular media. *Geophysical Journal International*, *181*(3), 1480-1498.

928

929   81. Revil, A., & Skold, M. (2011). Salinity dependence of spectral induced polarization in
930   sands and sandstones. *Geophysical Journal International*, *187*(2), 813-824.

931

82. Revil, A., Atekwana, E., Zhang, C., Jardani, A., & Smith, S. (2012). A new model for the spectral induced polarization signature of bacterial growth in porous media. *Water Resources Research*, *48*(9).

83. Revil, A., Florsch, N., & Mao, D. (2015a). Induced polarization response of porous media with metallic particles—Part 1: A theory for disseminated semiconductors. *Geophysics*, *80*(5), D525-D538.

84. Revil, A., Abdel Aal, G. Z., Atekwana, E. A., Mao, D., & Florsch, N. (2015b). Induced polarization response of porous media with metallic particles—Part 2: Comparison with a broad database of experimental data. *Geophysics*, *80*(5), D539-D552.

85. Revil, A., Coperey, A., Shao, Z., Florsch, N., Fabricius, I. L., Deng, Y., ... & van Baaren, E. S. (2017). Complex conductivity of soils. *Water Resources Research*, *53*(8), 7121-7147.

86. Rosier, C. L., Atekwana, E. A., Aal, G. A., & Patrauchan, M. A. (2019). Cell concentrations and metabolites enhance the SIP response to biofilm matrix components. *Journal of Applied Geophysics*, *160*, 183-194.

87. Schurr, J. M. (1964). On the theory of the dielectric dispersion of spherical colloidal particles in electrolyte solution1. *The Journal of Physical Chemistry*, *68*(9), 2407-2413.

88. Schwartz, N., & Furman, A. (2014). On the spectral induced polarization signature of soil organic matter. *Geophysical Journal International*, *200*(1), 589-595.

89. Schwartz, N., Shalem, T., & Furman, A. (2014). The effect of organic acid on the spectral-induced polarization response of soil. *Geophysical Journal International*, *197*(1), 269-276.

90. Schwarz, G. (1962). A theory of the low-frequency dielectric dispersion of colloidal particles in electrolyte solution1, 2. *The Journal of Physical Chemistry*, *66*(12), 2636-2642.

966   91. Seigel, H., Nabighian, M., Parasnis, D. S., & Vozoff, K. (2007). The early history of
967   the induced polarization method. *The Leading Edge*, *26*(3), 312-321.
968

969   92. Slater, L., & Atekwana, E. (2013). Geophysical signatures of subsurface microbial
970   processes. *Eos, Transactions American Geophysical Union*, *94*(8), 77-78.
971

972   93. Slater, L., & Binley, A. (2006). Synthetic and field-based electrical imaging of a
973   zerovalent iron barrier: Implications for monitoring long-term barrier performance.
974   *Geophysics*, *71*(5), B129-B137.
975

976   94. Slater LD, & Reeve A (2002) Investigating peatland stratigraphy and hydrogeology
977   using integrated electrical geophysics. Geophysics 67(2):365–378
978

979   95. Slater, L., Binley, A. M., Daily, W., & Johnson, R. (2000). Cross-hole electrical imaging
980   of a controlled saline tracer injection. *Journal of applied geophysics*, *44*(2-3), 85-102.
981

982   96. Slater, L., Ntarlagiannis, D., Personna, Y. R., & Hubbard, S. (2007). Pore-scale spectral
983   induced polarization signatures associated with FeS biomineral transformations.
984   *Geophysical Research Letters*, *34*(21).
985

986   97. Strohmeier, S., Knorr, K. H., Reichert, M., Frei, S., Fleckenstein, J. H., Peiffer, S., &
987   Matzner, E. (2013). Concentrations and fluxes of dissolved organic carbon in runoff
988   from a forested catchment: insights from high frequency measurements. *Biogeosciences*,
989   *10*(2), 905.
990

991   98. Tamura, H., Goto, K., Yotsuyanagi, T., & Nagayama, M. (1974). Spectrophotometric
992   determination of iron (II) with 1, 10-phenanthroline in the presence of large amounts
993   of iron (III). *Talanta*, *21*(4), 314-318.
994

995   99. Trappe, J., & Kneisel, C. (2019). Geophysical and sedimentological investigations of
996   Peatlands for the assessment of lithology and subsurface water pathways.
997   *Geosciences*, *9*(3), 118.
998

999   100.   Tsukanov, K., & Schwartz, N. (2020). Relationship between wheat root
1000   properties and its electrical signature using the spectral induced polarization method.
1001   *Vadose Zone Journal*, *19*(1), e20014.

1002

1003   101.   Uhlemann, S.S., Sorensen, J.P.R., House, A.R., Wilkinson, P.B., Roberts, C.,
1004   Gooddy, D.C., Binley, A.M. and Chambers, J.E., 2016. Integrated time-lapse
1005   geoelectrical imaging of wetland hydrological processes. *Water Resources Research*,
1006   *52*(3), pp.1607-1625.

1007

1008   102.   Ulrich, C., & Slater, L. (2004). Induced polarization measurements on
1009   unsaturated, unconsolidated sands. *Geophysics*, *69*(3), 762-771.

1010

1011   103.   Urban, N. R. Retention of sulfur in lake-sediments. in *Environmental Chemistry
1012   of Lakes and Reservoirs* (ed. Baker, L. A.) (American Chemical Society, 1994). **237**,
1013   323–369

1014

1015   104.   Wainwright, H. M., Flores Orozco, A., Bücker, M., Dafflon, B., Chen, J.,
1016   Hubbard, S. S., & Williams, K. H. (2016). Hierarchical Bayesian method for mapping
1017   biogeochemical hot spots using induced polarization imaging. *Water Resources
1018   Research*, *52*(1), 533-551.

1019

1020   105.   Wang, Y., Wang, H., He, J. S., & Feng, X. (2017). Iron-mediated soil carbon
1021   response to water-table decline in an alpine wetland. *Nature communications*, *8*(1), 1-
1022   9.

1023

1024   106.   Ward, S. H. (1988, January). The resistivity and induced polarization methods.
1025   In *Symposium on the Application of Geophysics to Engineering and Environmental
1026   Problems 1988* (pp. 109-250). Society of Exploration Geophysicists.

1027

1028   107.   Waxman, M. H., & Smits, L. J. M. (1968). Electrical conductivities in oil-
1029   bearing shaly sands. *Society of Petroleum Engineers Journal*, *8*(02), 107-122.

1030

1031   108.   Weigand, M., & Kemna, A. (2017). Multi-frequency electrical impedance
1032   tomography as a non-invasive tool to characterize and monitor crop root systems.
1033   *Biogeosciences*, *14*(4).

1034

1035   109.   Weller, A., Zhang, Z. and Slater, L., 2015. High-salinity polarization of
1036   sandstones. *Geophysics*, *80*(3), pp.D309-D318.

1037

1038   110.   Williams, K. H., Ntarlagiannis, D., Slater, L. D., Dohnalkova, A., Hubbard, S.
1039   S., & Banfield, J. F. (2005). Geophysical imaging of stimulated microbial
1040   biomineralization. *Environmental science & technology*, *39*(19), 7592-7600.

1041

1042   111.   Williams, K. H., Kemna, A., Wilkins, M. J., Druhan, J., Arntzen, E., N'Guessan,
1043   A. L., ... & Banfield, J. F. (2009). Geophysical monitoring of coupled microbial and
1044   geochemical processes during stimulated subsurface bioremediation. *Environmental
1045   science & technology*, *43*(17), 6717-6723.

1046

1047   112.   Wong, J. (1979). An electrochemical model of the induced-polarization
1048   phenomenon in disseminated sulfid ores. *Geophysics*, *44*(7), 1245-1265.

1049

1050   113.   Zhang, C., Ntarlagiannis, D., Slater, L., & Doherty, R. (2010). Monitoring
1051   microbial sulfate reduction in porous media using multipurpose electrodes. *Journal of
1052   Geophysical Research: Biogeosciences*, *115*(G3).

1053

1054   114.   Zhang, C., Slater, L., & Prodan, C. (2013). Complex dielectric properties of
1055   sulfate-reducing bacteria suspensions. *Geomicrobiology Journal*, *30*(6), 490-496.

1056

1057   115.   Zimmermann, E., Kemna, A., Berwix, J., Glaas, W., & Vereecken, H. (2008).
1058   EIT measurement system with high phase accuracy for the imaging of spectral induced
1059   polarization properties of soils and sediments. *Measurement Science and Technology*,
1060   *19*(9), 094010.

1061

1062   116.   Zimmermann, E., Huisman, J. A., Mester, A., & van Waasen, S. (2019).

1063   Correction of phase errors due to leakage currents in wideband EIT field measurements

1064   on soil and sediments. *Measurement Science and Technology*, *30*(8), 084002.

1065